nature structural & molecular biology

ARTICLES

https://doi.org/10.1038/s41594-019-0224-z

Receptor subtype discrimination using extensive shape complementary designed interfaces

Luke T. Dang[1,2,3,11], Yi Miao[4,5,6,11], Andrew Ha[7], Kanako Yuki[7], Keunwan Park[8], Claudia Y. Janda[4,5,6,10], Kevin M. Jude[4,5,6], Kritika Mohan[4,5,6], Nhi Ha[7], Mario Vallon[7], Jenny Yuan[7], José G. Vilches-Moure[9], Calvin J. Kuo[7], K. Christopher Garcia[4,5,6*] and David Baker[1,2,3*]

To discriminate between closely related members of a protein family that differ at a limited number of spatially distant positions is a challenge for drug discovery. We describe a combined computational design and experimental selection approach for generating binders targeting functional sites with large, shape complementary interfaces to read out subtle sequence differences for subtype-specific antagonism. Repeat proteins are computationally docked against a functionally relevant region of the target protein surface that varies in the different subtypes, and the interface sequences are optimized for affinity and specificity first computationally and then experimentally. We used this approach to generate a series of human Frizzled (Fz) subtype-selective antagonists with extensive shape complementary interaction surfaces considerably larger than those of repeat proteins selected from random libraries. In vivo administration revealed that Wnt-dependent pericentral liver gene expression involves multiple Fz subtypes, while maintenance of the intestinal crypt stem cell compartment involves only a limited subset.

A challenge encountered frequently in drug discovery is targeting a small subset of the members of a closely related protein family to achieve a specific therapeutic outcome with minimal off-target toxicity[1]. For example, cytokine and growth factor receptor systems (such as interferons, Wnt, Notch, BMP)[2–6] often have multiple receptor subtypes with different biological roles. Current strategies for targeting specific receptor or ligand subtypes generally involve selection from randomized libraries utilizing counter-screening for desired specificity[7,8]. Using these methods, high affinity Ankyrin binders called designed ankyrin repeat proteins (DARPins) have been selected against a number of targets and show potential as therapeutics[9,10]. Although library selection methods are capable of obtaining high affinity binders, they remain empirical, and cannot explicitly target specific regions of a protein surface. Previous efforts to generate specific binders against similar targets has therefore required the independent evolution of binders against each target[7,8]. An alternative, potentially superior strategy would be to target specific regions of a protein surface that could enable 'reading out' of specificity between closely related homologs.

We reasoned that binding modes with extensive interface surfaces that span spatially distant variant positions could provide a general solution to the problem of discriminating between closely related members of a protein family. We developed a two-step approach for designing binding modes poised for high affinity, specificity and functional antagonism. First, we used computational design to target binding to a defined, large surface region of a family member that includes both the conserved functional site and the adjacent non-conserved residues. This computational sampling of structure space can survey the wide range of possible backbone orientations more broadly than selection methods owing to library size constraints. Second, we generated subtype-specific variants by exploiting contacts with subtype-specific positions within this broadly conserved buried interface. We chose repeat proteins as scaffolds owing to their modular and idealized architecture, which enables extension as needed for the design of larger interfaces. In addition, the favorable biochemical properties of these designed repeat protein binders (DRPBs) are ideal for downstream functional applications.

Results

Computational design of Fz subtype-specific DRPBs. We tested this approach on the Frizzled (Fz) family of Wnt receptors, an important example of a closely related set of therapeutic targets, as subtype-specific antagonism of Fz could reduce or limit off-target toxicity[11]. Dysregulation of Wnt signaling is widely implicated in cancer[12]. However, full elucidation of the role of the Wnt pathway in tissue homeostasis and disease has been limited by the availability of reagents that can modulate signaling in a receptor subtype-specific manner, as there are 19 distinct Wnt ligands and 10 Fz receptors (as well as other co-receptors, inhibitors, and agonists)[11,13]. Different tissues express different subsets of Fz, so there is a need for molecules with the ability to distinguish between Fz subtypes that are highly homologous in sequence. Indeed, highly cross-reactive anti-Fz monoclonal antibodies have been tested in clinical trials for several cancers but resulted in dose-limiting toxicity, including bone fractures (OncoMed Pharmaceuticals). Native Wnts do not provide good starting points for generating such binding reagents as they exhibit binding promiscuity for the different Fzs[14,15]. Furthermore, endogenous

[1]Department of Biochemistry, University of Washington, Seattle, WA, USA. [2]Institute for Protein Design, University of Washington, Seattle, WA, USA. [3]Howard Hughes Medical Institute, University of Washington, Seattle, WA, USA. [4]Department of Molecular and Cellular Physiology, Stanford University School of Medicine, Stanford, CA, USA. [5]Department of Structural Biology, Stanford University School of Medicine, Stanford, CA, USA. [6]Howard Hughes Medical Institute, Stanford University School of Medicine, Stanford, CA, USA. [7]Department of Medicine, Division of Hematology, Stanford University School of Medicine, Stanford, CA, USA. [8]Systems Biotechnology Research Center, Korea Institute of Science and Technology, Gangneung, Republic of Korea. [9]Department of Comparative Medicine, Stanford University School of Medicine, Stanford, CA, USA. [10]Present address: Princess Máxima Center for Pediatric Oncology, Utrecht, The Netherlands. [11]These authors contributed equally: Luke T. Dang and Yi Miao. *e-mail: kcgarcia@stanford.edu; dabaker@uw.edu

Wnts are lipidated, and not water-soluble, rendering them impractical to re-engineer for functional applications. We reasoned that the discrimination of subtle sequence differences between different Fzs (Fig. 1a,b, and Supplementary Notes, page 18) could be achieved using repeat proteins such as Ankyrins, which have extended concave surfaces roughly complementary to the convex surface adjacent to the lipid binding cleft of the Fz cysteine-rich domain (CRD) structure[9,15].

We therefore sought to develop high-affinity subtype-specific Fz binders with extensive interfaces that included primary contacts with both the conserved lipid-binding cleft (to enable Wnt antagonism) as well as secondary contacts against adjacent positions that are variable between receptor subtypes (to enable development of orthogonal binding specificities). As random library selection methods do not enable such precise targeting (Fig. 1c), we utilized computational docking and design methods starting from an idealized Ankyrin scaffold (PDB: 4GPM) optimized previously using Rosetta. Each repeat is identical in this design, and it is very stable; because it is designed using Rosetta it has very low energy in the Rosetta force field, which makes the subsequent interface design calculations more straightforward as energy optimization will change the sequence only to make new interactions with the target[16,17]. The scaffold was globally docked against the Fz8 surface. Binding modes that inserted loops into the Wnt lipid binding groove and encompassed adjacent variable regions, and had large interface surface areas with high backbone shape complementarity were selected. The interfaces of selected binding conformations were computationally optimized for low energy interactions with Fz8CRD. 22 designs with high shape complementarity (average SC of 0.70) and extensive buried surface area (BSA) (average >2,400 Å^2) (Fig. 1d,e and Supplementary Notes, page 27) were produced and tested, but did not bind Fz with detectable affinity. As we reasoned that there was a possibility of design errors over the extensive buried interface that could limit initial binding detection. To achieve high affinity ligands, we screened for Fz binding through error-prone PCR mutagenesis on the selected designs, and generated libraries via yeast surface display[18,19]. Following further sequence optimization, a final clone DRPB_Fz8 specifically bound Fz5 with a K_d of 220 pM as measured by biolayer interferometry (BLI) (Supplementary Notes, pages 19 and 30), competed for Fz binding with a protein designed previously, B12 (ref. [20]) and an anti-Fz scFv[14] (Supplementary Notes, page 20), and is thermostable to 80 °C (Supplementary Notes, page 19). DRPB_Fz8 has essentially equal affinity for the very closely related Fz8 subtype members, Fz5 and Fz8, (Supplementary Fig. 1 and Supplementary Notes, page 33) and we used them interchangeably in these initial binding and optimization experiments, depending on availability.

DRPB_Fz8–Fz8CRD complex structure confirms computational design and paves the way for specificity tuning. To confirm our design, a 2.3 Å structure of the DRPB_Fz8-Fz8CRD complex was solved, revealing a binding mode that is virtually identical to the 'fingers-in-groove' or 'grasping-hand' design model (backbone RMSD 1.6 Å). This interaction fully occludes the Fz lipid binding groove, preventing binding to the native Wnt lipid, thus acting as an antagonist (Fig. 2 and Supplementary Fig. 1). A difference between the DRPB_Fz8-Fz8CRD crystal structure and the original computational model is a narrowing of the receptor cleft upon binding owing to shifting of the adjacent Fz alpha helix. Although it was accommodated in the computational model, Phe42 is incompatible with the narrowed conformation of the helical backbone in the crystal structure (Supplementary Fig. 1d); removing this bulky hydrophobic group restores the underlying designed high-affinity interface. The single point mutations Phe42Ala and Thr66Ser, individually provided only weak binding affinity to the target, but the double substitution led to high affinity binding (Supplementary Fig. 1a).

We subsequently redesigned DRPB_Fz8 for specific binding to the other two major Fz subtypes, Fz7 (Fz1/2/7) and Fz4, using a targeted library approach. To guide library construction, we built comparative models for Fz4 and Fz7 using Rosetta, aligned them to Fz8 in the DRPB_Fz8–Fz8CRD crystal structure, and carried out Rosetta design calculations to identify amino acid substitutions on DRPB_Fz8 that increase affinity for Fz4 and Fz7. In parallel, we generated a site saturation mutagenesis library containing point mutations to all residues of DRPB_Fz8, carried out selections towards Fz4 and Fz7, and identified enriched positions via next-generation sequencing (Supplementary Notes, pages 21 and 22)[19]. Substitutions suggested by both the computational and experimental data were combined to generate focused libraries targeting Fz4 and Fz7 subtypes (Supplementary Notes, pages 31 and 32). Sorting of the Fz7 subtype yeast library yielded a biased yet cross-reactive clone named DRPB_Fz7/8, which binds to Fz7 and Fz8 subtypes (Fig. 3a and Supplementary Fig. 2). Furthermore, a Fz7 subtype-specific clone, DRPB_Fz7 (Fig. 3b and Supplementary Notes, page 23), was isolated from an error-prone yeast library based on the DRPB_Fz7/8 scaffold. Similarly, sorting of the Fz4 targeted library yielded a Fz4 subtype-specific clone, DRPB_Fz4 (Supplementary Notes, page 24), which binds with a K_d of 1.4 nM to Fz4 (Fig. 3c, Supplementary Notes, pages 23–25, and Supplementary Fig. 3).

Complex structures of DRPB-Fz explain Fz subtype specificity. To dissect the molecular mechanism of DRPB affinity and specificity tuning, we determined the structures of all DRPB-FzCRD complexes (Fig. 3 and Table 1). Structural superposition of DRPB_Fz8-Fz8CRD with DRPB_Fz7/8-Fz7CRD revealed a key Ala111Asp mutation from DRPB_Fz8 to DRPB_Fz7/8, enabling hydrogen bond and salt bridge formation with a corresponding Lys of Fz7, which is a Glu in the Fz8 subtype (Fig. 3a and Supplementary Fig. 4a,b). The structure of Fz7-specific DRPB_Fz7 with Fz7CRD highlighted an Ala108Asp mutation, which clashes with Trp73 in the Fz8 subtype, whereas this mutation is tolerated in the Fz7 subtype owing to the smaller sidechain of Tyr (Fig. 3b and Supplementary Fig. 4c), explaining the enhanced specificity. The complex structure of DRPB_Fz4 in Fz4 CRD revealed a limited repositioning of DRPB_Fz4 compared with DRPB_Fz8, albeit with a globally preserved binding mode; structural analysis suggested that a combination of residues modulate the specificity change (Fig. 3c and Supplementary Fig. 5). Thus, we have engineered DRPB antagonists to three major Fz subtypes using a designed, functionally targeted binding mode with high shape complementarity and large BSA, allowing us to distinguish between Fz isoforms. The successful re-engineering of binding specificity marks significant progress towards development of a suite of proteins with orthogonal binding specificities utilizing a pre-designed binding mode.

Fz subtype-specific DRPB antagonists inhibit homeostasis of the intestinal crypt stem cell compartment and expression of liver Wnt target genes. Despite pleiotropic involvement of Wnt signaling in stem cell biology and tissue homeostasis, genetic redundancy among the 10 *Fz* genes has greatly hindered the identification of essential functionality of *Fz* gene(s) in adult tissue compartments[11,13]. Therefore, systematic Fz subtype-specific inhibition, as with the DRPB antagonists, represents a robust pharmacologic solution to the quandary of functional interrogation of Fz receptors in vivo. Lgr5$^+$ intestinal stem cells predominantly express Fz5 and Fz7, and to a lesser degree Fz1, Fz2, Fz6, Fz8, and Fz9 (ref. [21]); this redundancy is likely to underlie the inability of any single or combinatorial *Fz* knockout to demonstrate an adult homeostatic intestinal phenotype.

To probe the Fz subtype-specific antagonist function of these DRPBs, we first treated cell lines with predominant expression of Fz2, Fz4, or Fz5 with DRPBs while stimulating with Wnt3a conditioned media. These Fz-selective DRPBs showed potent Fz subtype-specific inhibition of Wnt signaling, as demonstrated by TopFlash

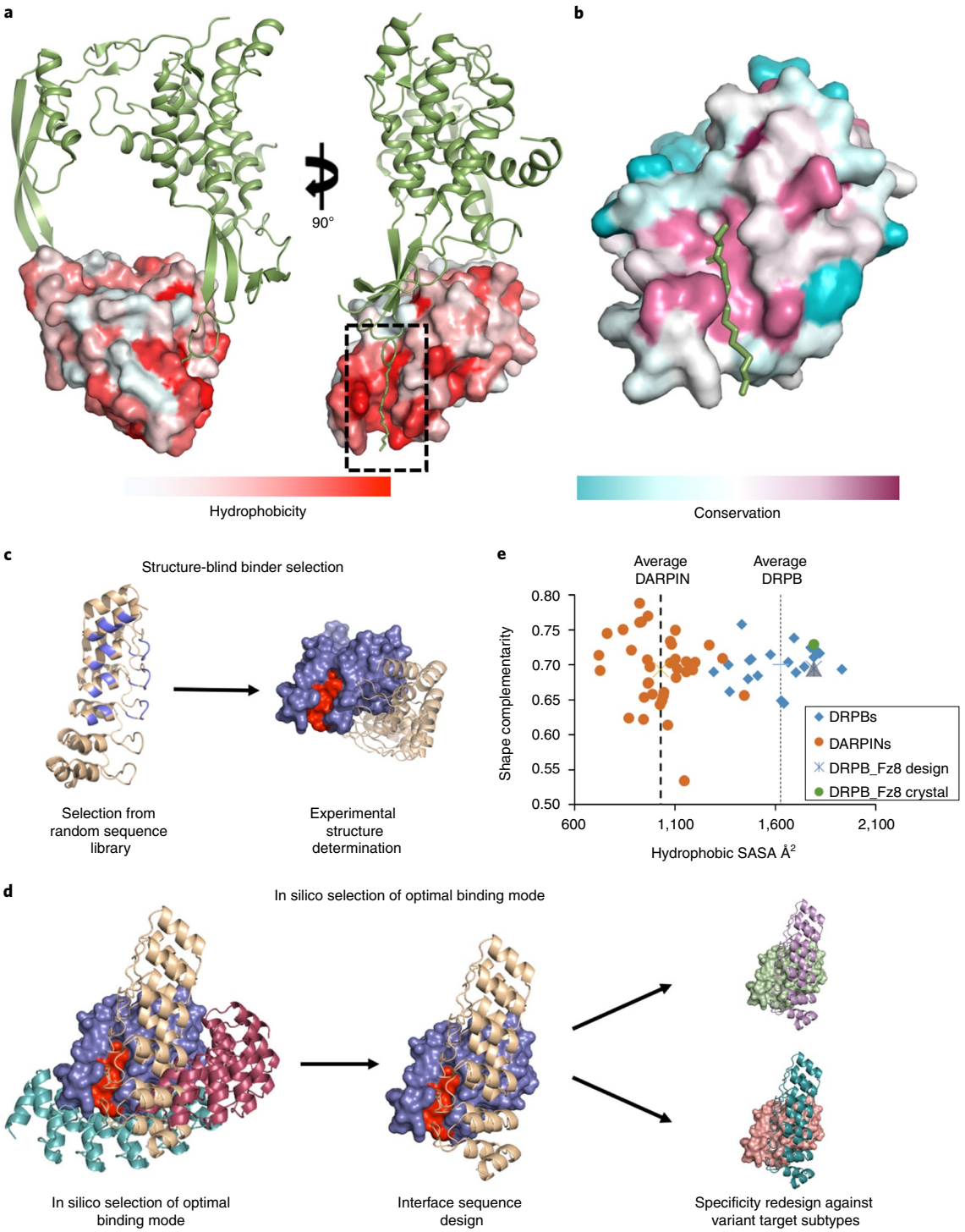

Fig. 1 | Computational design of Fz subtype-specific DRPBs. a, Native *Xenopus* Wnt8(XWnt8)–Fz8CRD complex depicting the essential functional interactions including the deep positioning of the Wnt lipid group (sticks) into the Fz hydrophobic lipid binding groove. XWnt8 is shown in green, and Fz8CRD is colored according to hydrophobicity. **b**, Structure of six human Fz CRDs colored according to conservation with the highest conservation colored in magenta as seen in the Fz hydrophobic groove, adjacent positions are less well conserved. **c**,**d**, Differences between the in silico method for selecting binding modes for DRPBs and binder selection from randomized libraries. Traditional, empirical methods (**c**) mutagenize scaffold surface residues, select the randomized library for binding (**c**, left), and then experimentally determine the binding mode after affinity maturation (**c**, right), often revealing a binding footprint incompatible with functional activity. In the computational, structure-guided design of DRPBs (**d**), optimal backbone conformations are discovered by exhaustive computational docking of a scaffold (ankyrin) against the target (blue). Optimal shape complementary binding modes are selected rationally to maximize functional blockade and include extensive coverage of adjacent variant regions (**d**, left). The interface of the selected binding mode is then computationally optimized (**d**, middle). Redesign involves engineering of orthogonal subtype specificities via substitution of the target structure with related structures and subsequent further redesign (**d**, right). DRPBs (dotted line) generated with this computational approach (**e**) have significantly larger hydrophobic buried solvent accessible surface areas (Å^2) than typical monomeric DARPin interfaces (dashed line), but notably retain similar shape complementarity across these larger interfaces.

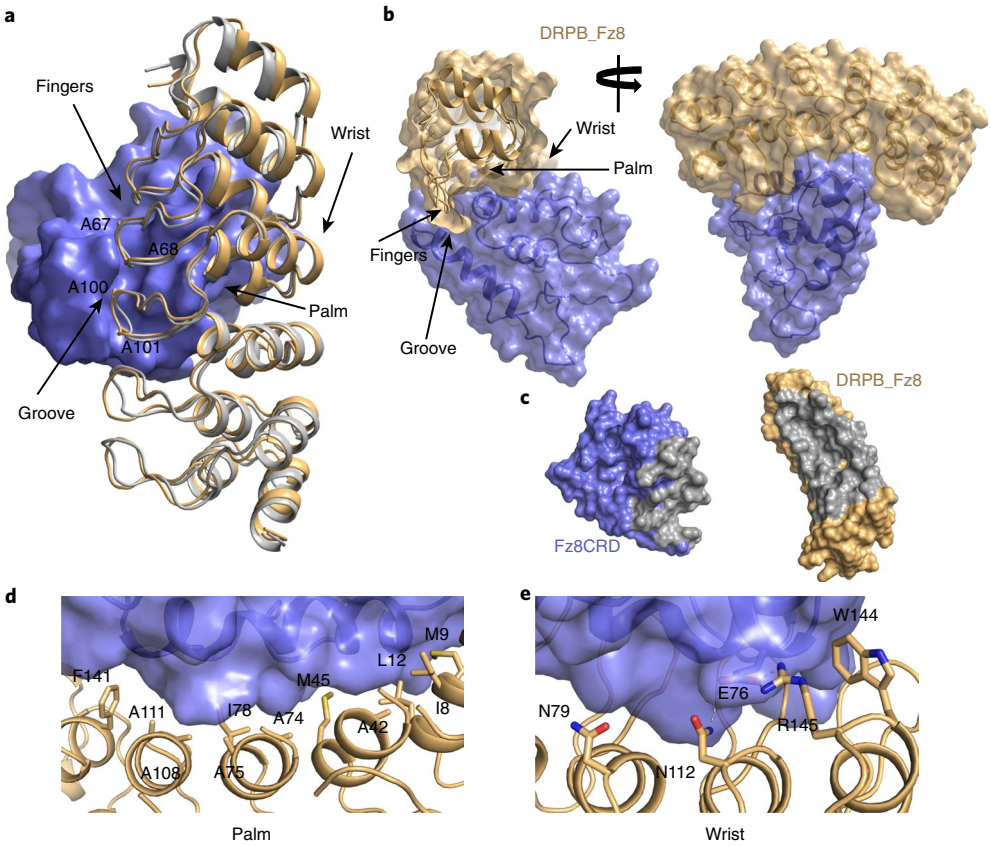

Fig. 2 | DRPB_Fz8–Fz8CRD complex structure confirms computational design and paves the way for specificity tuning. a, The crystal structure of Fz8CRD complexed with DRPB_Fz8 (light orange) matches the computationally designed complex (grey). The Fz8CRD is shown by the blue surface. The Ala 'fingers' of DRPB_Fz8 deeply 'grasp' the hydrophobic groove of Fz8CRD. **b**, Overall structures of DRPB_Fz8 with Fz8CRD. **c**, An 'open-book' view showing the interacting surface on both Fz8CRD and DRPB_Fz8. The interacting surface on Fz8CRD and DRPB_Fz8 is colored in grey. **d**, The 'palm' region of DRPB_Fz8 consists of hydrophobic residues that make van der Waals interactions with Fz8 CRD. The 'fingers' region of DRPB_Fz8 is omitted to gain a clear view. **e**, The 'wrist' region of DRPB_Fz8 consists of hydrophilic and charged residues that contribute to both solubility and receptor recognition. The DRPB_Fz8 Asn112 and Arg145 form hydrogen bonds and salt bridges with Glu76 of Fz8CRD, shown as grey dashed lines.

reporter (Supplementary Fig. 6). We then assessed the antagonist function of DRPBs during in vitro intestinal organoid growth. As duodenal organoids produce endogenous Wnts, which are essential for their growth, organoid growth is a stringent readout for DRPB inhibitory activity. Both human and mouse duodenum organoid cultures were cultured with all four types of DRPBs. Both DRPB_Fz4 and DRPB_Fz7 showed no effects (Fig. 4a). DRPB_Fz8 strongly inhibited organoid growth in the 0.1–1 nM range, but several log higher concentrations of DRPB_Fz7/8 was required (Supplementary Fig. 7a,b), consistent with the stronger Fz5 and Fz8 affinity of DRPB_Fz8 versus DRPB_Fz7/8 (Supplementary Fig. 3). For in vivo studies, we fused the DRPBs to mouse serum albumin (MSA) to extend the circulating half-life. Notably, daily intravenous administration of MSA-DRPB_Fz8 but not the other DRPBs induced profound loss of crypts and villi within 7 d (Fig. 4b and Supplementary Fig. 7), consistent with blockade of canonical Wnt signaling via Dkk1 or Porcupine inhibitors[21–23]. We reasoned that the lack of effect of MSA-DRPB_Fz7/8 on duodenal homeostasis could be due to lower Fz5 and Fz8 binding affinity versus MSA-DRPB_Fz8, as reflected in organoid culture. To overcome this, we generated recombinant adenoviruses expressing each of the DRPBs, as intravenous adenovirus injection infects the mouse liver and allows continuous high-level hepatic secretion of transgene products into the circulation for weeks[21,24]. Accordingly, adenoviruses expressing DRPB_Fz7/8 and DRPB_Fz8 both produced rapid duodenal crypt and villus loss resulting in weight loss and lethality within 7 d, while DRPB_Fz4 and DRPB_Fz7 were ineffective despite robust serum expression of each DRPB (Fig. 4c and Supplementary Fig. 8). The ability of the restricted spectrum DRPB_Fz8 to elicit catastrophic crypt and villus loss strongly implicates Fz5 and/or Fz8 function during intestinal homeostasis with much stronger phenotypes that have been observed with individual Fz receptor genetic deletion[25].

The liver represents an additional Wnt-sensitive compartment, with Wnt pathway gain or loss of function profoundly altering zonated expression of liver genes[20,26]. Adenoviruses expressing each of the four DRPBs, or negative control adenovirus were tested for effects on the Wnt-responsive genes *Glul* (glutamine synthetase) and *Axin2*. Although negative control adenovirus liver (Adeno-Fc) expressed GLUL in a highly characteristic pericentral zone, adenovirus-expressed DRPB_Fz4, DRPB_Fz7 and DRPB_Fz8 partially repressed GLUL, and notably DRPB_Fz7/8 completely repressed GLUL (Fig. 4d,e). This was strongly paralleled by the complete repression of liver *Glul* and *Axin2* mRNA by DRPB_Fz7/8 with more intermediate inhibition seen with DRPB_Fz4, DRPB_Fz7 and DRPB_Fz8 (Fig. 4f,g). Thus, in contrast to the comparatively narrow Fz functional spectrum of intestinal homeostasis, Wnt-dependent liver gene expression appears to require the broad-based contribution of diverse Fz receptor subtypes. Our strategy therefore enables 'tuning' of Fz specificity based on tissue expression of the Fz subtypes.

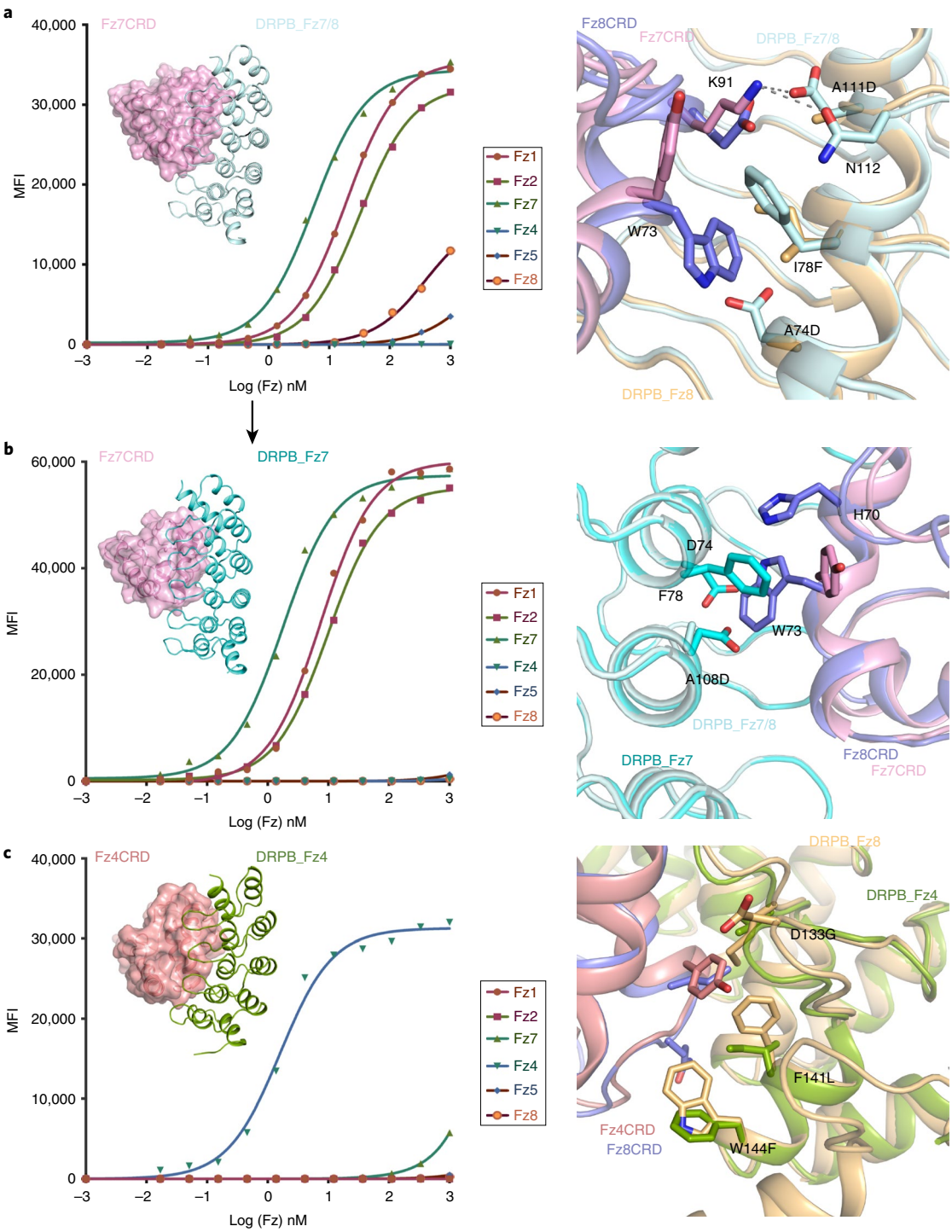

Fig. 3 | Structures of DRPB-Fz complexes explain Fz subtype specificity. a, Titration of DRPB_Fz7/8 to biotinylated Fz1, Fz2, Fz4, Fz5, Fz7 and Fz8 CRDs. DRPB_Fz8 was displayed on the surface of yeast. The levels of bound FzCRDs were quantified using Alexa Fluor 647 conjugated streptavidin and the mean fluorescence intensity (MFI) was analyzed and plotted in GraphPad Prism 7. DRPB_Fz7/8 showed an EC_{50} (half-maximum effective concentration) of 19.0, 31.6 and 5.6 nM for Fz1, Fz2 and Fz7. DRPB_Fz7/8 showed weaker staining to Fz5 and Fz8 with EC_{50} not available. Representative Ala111Asp mutation from DRPB_Fz8 to DRPB_Fz7/8 allows hydrogen bond and salt bridge formation between DRPB_Fz7/8 and Fz7 Lys91, shown by grey dashed lines. DRPB_Fz7/8 is shown in pale cyan, Fz7CRD in pink, and Fz8CRD in slate. The corresponding position of Lys91 is Glu, weakening the DRPB_Fz7/8 interaction with the Fz8 subtype. **b**, DRPB_Fz7 showed strong binding to Fz1, Fz2, and Fz7. DRPB_Fz7 showed no cross-reactivity to Fz5 and Fz8 up to 1 μM concentration (Table 1 and Supplementary Notes, page 5). The Ala108Asp mutation from DRPB_Fz7/8 to DRPB_Fz7 leads to steric clashes with Trp73 of Fz8 CRD. On the other hand, the corresponding position of Fz7 subtype is Tyr, whose less bulky sidechain allows it to take a different rotamer conformation. This Ala108Asp mutation thus further confers specificity to the Fz7 subtype by eliminating Fz8 binding. DRPB_Fz7/8 is shown in light cyan, and DRPB_Fz7 in cyan. **c**, DRPB_Fz4 only binds to Fz4 with an EC_{50} of 1.6 nM. DRPB_Fz4–Fz4CRD showed backbone movement compared with DRPB_Fz8–Fz8CRD. Therefore, DRPB_Fz4 and Fz4CRD were individually superpositioned with DRPB_Fz8 and Fz8CRD. The differences between DRPB_Fz4 and DRPB_Fz8 surface led to less favorable interactions between DRPB_Fz4 and Fz8. For example, Asp133Gly, Phe141Ile, and Trp144Phe weaken interactions to Fz8CRD owing to less bulky sidechains. The yeast titration experiements were repeated once with similar results.

Table 1 | Data collection and refinement statistics (molecular replacement)

	DRPB_Fz8 + Fz8CRD (PDB: 6NDZ)	DRPB_Fz7/8 + Fz7CRD (PDB: 6NE2)	DRPB_Fz4 + Fz4CRD (PDB: 6NE1)	DRPB_Fz7 + Fz7CRD (PDB: 6NE4)
Data collection				
Space group	P 2_1 2_1 2_1	P 2 2_1 2_1	P 2 2_1 2_1	P 2 2_1 2_1
Cell dimensions				
a, *b*, *c* (Å)	79.9, 109.0, 114.4	57.6, 68.0, 86.4	51.8, 62.6, 86.2	57.6, 68.4, 86.5
α, β, γ (°)	90, 90, 90	90, 90, 90	90, 90, 90	90, 90, 90
Resolution (Å)	50.0–2.22 (2.26–2.22)[a]	45.0–1.30 (1.38–1.30)	50.0–3.00 (3.05–3.00)	50.0–1.65 (1.68–1.65)
R_{merge}	0.14 (0.92)	0.054 (0.65)	0.16 (0.82)	0.084 (0.72)
$I/\sigma(I)$	26.8 (1.2)	16.2 (1.4)	10.8 (1.0)	38.1 (2.3)
$CC_{1/2}$	1 (0.58)	1 (0.61)	1 (0.66)	1 (0.80)
Completeness (%)	93.5 (70.8)	99.0 (93.9)	99.0 (91.5)	99.8 (99.6)
Redundancy	10.5 (3.8)	7.0 (3.6)	5.6 (3.3)	11.9 (10.0)
Refinement				
Resolution (Å)	41.9–2.26 (2.35–2.26)	39.2–1.30 (1.35–1.30)	43.1–3.01 (3.12–3.01)	34.2–1.65 (1.71–1.65)
No. reflections	44466	83589	5863	41811
R_{work} / R_{free}	0.212/0.238	0.161/0.184	0.234/0.293	0.160/0.186
No. atoms				
Protein	7011	2368	2028	2358
Ligand/ion	56 (MPD, ACT, ACY)	108 (ACT, SO4, EDO, NAG)	28 (NAG)	78 (SO4, EDO)
Water	216	268	6	274
B factors				
Protein	73.5	23.2	74.9	28.5
Ligand/ion	90.6	42.1	116.9	62.9
Water	59.4	33.9	34.0	41.0
R.m.s. deviations				
Bond lengths (Å)	0.003	0.007	0.004	0.014
Bond angles (°)	0.94	0.97	1.02	1.33

6NDZ data are collected from two protein crystals and the others are collected from a single crystal. [a]Values in parentheses are for highest-resolution shell.

Discussion

It is instructive to compare the structure of our designed complex to those of DARPin protein complexes obtained using library selection methods. Our DRPB is larger than most DARPins of known structure, and the binding interface in the DRPB-target designed complex is significantly larger than the single domain DARPin protein complexes in the Protein Data Bank (PDB) (Fig. 1e). However, despite the much larger surface area, the overall shape complementarity is very similar. Large shape complementary interfaces are difficult to obtain by traditional random library selection, as only a small fraction of the available sequence space can be searched, and hence favorable interactions throughout the interface are much less likely than for smaller interfaces. The difficulty of empirically selecting interfaces with such large surface area becomes clear when considering the increase in combinatorial diversity accompanying increasing interface size. For example, the DRPB initially designed here has 32 interface contacting residues mutated from the original scaffold. A full coverage library sampling these positions that includes all twenty amino acids at each site would represent a diversity of 20^{32} or 4.29×10^{41}, dwarfing the screening capabilities of current yeast, phage, or ribosome display methods. Libraries in which only a subset of the interface residues are varied can be made, but several of the residues kept constant are likely to be incompatible with binding, and hence large interfaces are unlikely to be obtained by selection. Computation can explicitly identify binding modes with large shape complementary interfaces, and optimize the sequence to be complementary to the target surface. However, computational protein design is still far from perfect, and purely computational approaches are not free of the challenges associated with large interfaces, as illustrated by the inclusion of the problematic Phe in the initial design—the large interface area increases the likelihood of locally incorrect modeling. Hence the combination of computation to define the overall binding mode with experimental optimization to resolve inaccuracies due to conformational changes (the narrowing of the Fz groove in the complex, for example) or other modeling errors, is particularly powerful. The designed binding mode, with 'hand-in-groove' insertion of ankyrin loops into the Fz lipid binding groove, is well suited to distinguish between closely related Fz subtypes with high affinity owing to the large, hydrophobic interface that makes contacts with both spatially disparate variant residues and core conserved regions. The principal advantages of our approach over traditional selection methods are: (1) the ability to generate much larger shape complementary binding interfaces, and (2) the ability to target these binding interfaces to functional regions encompassing sequence diversity among receptor subtypes.

Our design protocol can be broadly generalized to other ligand–receptor or protein–protein systems, with particular utility for challenging applications in which high affinity binding is insufficient and specific backbone placement is required for functional activity and specificity. The use of repeat proteins facilitates the design of custom binders with extensive interfaces to specification in such cases. Specific pharmacologic inhibition of these Wnt receptors by our approach provides a dose-dependent, robust tool for precise interrogation of Wnt signaling in a range of key processes. For

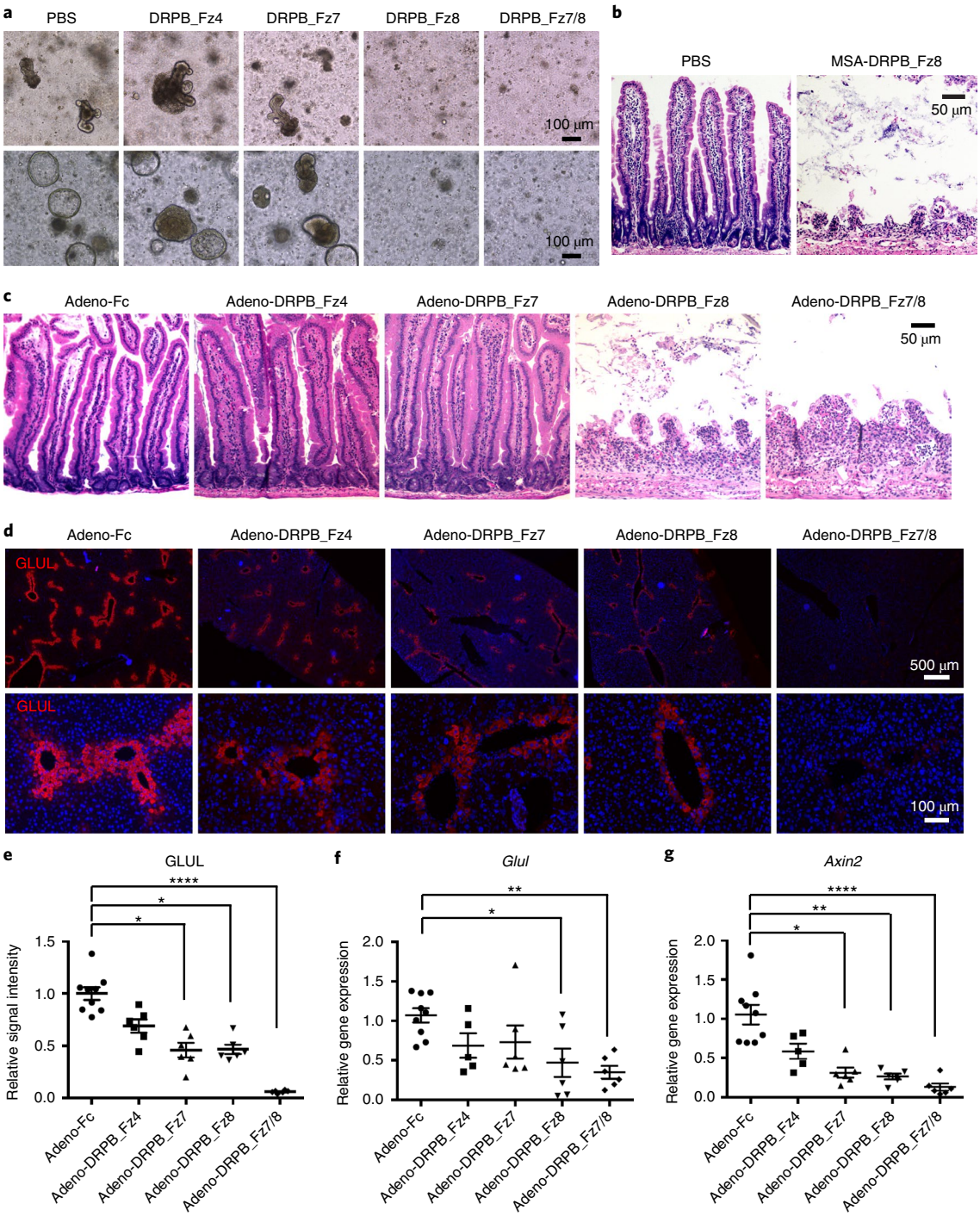

Fig. 4 | Fz subtype-specific DRPB antagonists inhibit homeostasis of the intestinal crypt stem cell compartment and expression of liver Wnt target genes. a, Mouse (top) and human (bottom) primary duodenal organoids that produce Wnt endogenously were cultured in submerged Matrigel in medium containing ENR (EGF/Noggin/R-spondin) with different Fz subtype-specific DRPB antagonist at 100 nM. The images were taken at day 7 (mouse) or day 10 (human) of continuous DRPB antagonist exposure. Each Fz antagonist was replenished every 3 d during medium change. In vitro experiments were repeated at least three times, and representative images are shown. **b**, In vivo phenotype following daily intravenous (i.v.) injections of recombinant MSA-DRPB_Fz8 at a concentration of 20 mg kg^{-1} or PBS for 7 d. H&E staining of jejunum is shown. The experiment was performed once due to limited protein yield. **c**,**d**, Representative images of H&E staining of jejunum cross-sections (**c**) and glutamine synthetase (GLUL, pericentral marker) immunofluorescence staining of livers (**d**) from mice that received adenoviruses expressing negative control IgG2a Fc (Fc) or different Fzsubtype-specific DRPB antagonist, 7 d post adenovirus injection (representative images from $n = 6$ to $n = 9$ mice per group; experiments were repeated twice). **e**, Quantification of the GLUL immunofluorescence signal intensity shown in **d**. **f**,**g**, Quantification of the *Glul* (**f**) and *Axin2* (**g**) transcript levels relative to *Gapdh* from liver samples (**d**) by qRT-PCR. Statistical analysis was performed using GraphPad Prism software. Data represent mean ± s.e.m. ($n = 9$ control and $n = 6$ for other groups; biological replicates from 2 experiments for all in vivo experiments (**c**–**g**)). Two-sided *P* values were calculated by Dunn's test of multiple comparisons following the Kruskal-Wallis test. $^{*}P < 0.05$, $^{**}P < 0.01$, $^{****}P < 0.0001$.

example, while redundancy has complicated the association of the 10 distinct *Fz* genes with specific biological processes, our studies suggest predominant relevance of Fz5 and/or Fz8 to intestinal stem cell homeostasis but broad contributions of multiple Fz receptors to Wnt-driven liver zonation. Knockout studies have demonstrated previously a critical role for Fz5 and Fz8 in mouse retinal development, but the *Fz5* and *Fz8* double knockout is embryonic lethal[27], limiting further detailed study. This proof of principle marks significant progress in the combined application of computational design and selection methods to the development of protein–protein interfaces that enable the molecular recognition of closely related proteins for the elucidation of complex signaling networks and precise therapeutic intervention to minimize off-target effects. The design of extensive high affinity and specificity binding interfaces using computational methods alone is an outstanding challenge for computational protein design methods development.

Online content

Any methods, additional references, Nature Research reporting summaries, source data, statements of code and data availability are available at https://doi.org/10.1038/s41594-019-0224-z.

Received: 12 January 2019; Accepted: 3 April 2019;
Published online: 13 May 2019

References

1. Davis, M. I. et al. Comprehensive analysis of kinase inhibitor selectivity. *Nat. Biotechnol.* **29**, 1046 (2011).
2. Massague, J. TGF-beta signal transduction. *Annu. Rev. Biochem.* **67**, 753–791 (1998).
3. Luca, V. C. et al. Structural basis for Notch1 engagement of Delta-like 4. *Science* **347**, 847–853 (2015).
4. Artavanis-Tsakonas, S., Rand, M. D. & Lake, R. J. Notch signaling: cell fate control and signal integration in development. *Science* **284**, 770–776 (1999).
5. Mendoza, J. L. et al. The IFN-λ-IFN-λR1-IL-10Rβ complex reveals structural features underlying type III IFN functional plasticity. *Immunity* **46**, 379–392 (2017).
6. Spangler, J. B., Moraga, I., Mendoza, J. L. & Garcia, K. C. Insights into cytokine–receptor interactions from cytokine engineering. *Annu. Rev. Immunol.* **33**, 139–167 (2015).
7. Kummer, L. et al. Structural and functional analysis of phosphorylation-specific binders of the kinase ERK from designed ankyrin repeat protein libraries. *Proc. Natl Acad. Sci.* **109**, E2248–E2257 (2012).
8. Schilling, J., Schöppe, J. & Plückthun, A. From DARPins to LoopDARPins: novel LoopDARPin design allows the selection of low picomolar binders in a single round of ribosome display. *J. Mol. Biol.* **426**, 691–721 (2014).
9. Binz, H. K. et al. High-affinity binders selected from designed ankyrin repeat protein libraries. *Nat. Biotechnol.* **22**, 575 (2004).
10. Plückthun, A. Designed ankyrin repeat proteins (DARPins): binding proteins for research, diagnostics, and therapy. *Annu. Rev. Pharmacol. Toxicol.* **55**, 489–511 (2015).
11. Nusse, R. & Clevers, H. Wnt/β-catenin signaling, disease, and emerging therapeutic modalities. *Cell* **169**, 985–999 (2017).
12. Reya, T. & Clevers, H. Wnt signalling in stem cells and cancer. *Nature* **434**, 843 (2005).
13. Clevers, H. Wnt/β-catenin signaling in development and disease. *Cell* **127**, 469–480 (2006).
14. Gurney, A. et al. Wnt pathway inhibition via the targeting of Frizzled receptors results in decreased growth and tumorigenicity of human tumors. *Proc. Natl Acad. Sci.* **109**, 11717–11722 (2012).
15. Janda, C. Y., Waghray, D., Levin, A. M., Thomas, C. & Garcia, K. C. Structural basis of Wnt recognition by Frizzled. *Science* **337**, 59–64 (2012).
16. Rohl, C. A., Strauss, C. E., Misura, K. M. & Baker, D. in *Methods in Enzymology* Vol. 383 (New York: Academic Press, 2004).
17. Fallas, J. A. et al. Computational design of self-assembling cyclic protein homo-oligomers. *Nat. Chem.* **9**, 353 (2017).
18. Boder, E. T. & Wittrup, K. D. Yeast surface display for screening combinatorial polypeptide libraries. *Nat. Biotechnol.* **15**, 553 (1997).
19. Whitehead, T. A. et al. Optimization of affinity, specificity and function of designed influenza inhibitors using deep sequencing. *Nat. Biotechnol.* **30**, 543 (2012).
20. Janda, C. Y. et al. Surrogate Wnt agonists that phenocopy canonical Wnt and β-catenin signalling. *Nature* **545**, 234–237 (2017).
21. Yan, K. S. et al. Non-equivalence of Wnt and R-spondin ligands during Lgr5+intestinal stem-cell self-renewal. *Nature* **545**, 238–242 (2017).
22. Kuhnert, F. et al. Essential requirement for Wnt signaling in proliferation of adult small intestine and colon revealed by adenoviral expression of Dickkopf-1. *Proc. Natl. Acad. Sci.* **101**, 266–271 (2004).
23. Kabiri, Z. et al. Stroma provides an intestinal stem cell niche in the absence of epithelial Wnts. *Development* **141**, 2206–2215 (2014).
24. Wei, K. et al. A liver Hif-2α–Irs2 pathway sensitizes hepatic insulin signaling and is modulated by Vegf inhibition. *Nat. Med.* **19**, 1331 (2013).
25. van Es, J. H. et al. Wnt signalling induces maturation of Paneth cells in intestinal crypts. *Nat. Cell Biol.* **7**, 381 (2005).
26. Benhamouche, S. et al. Apc tumor suppressor gene is the "zonation-keeper" of mouse liver. *Dev. Cell* **10**, 759–770 (2006).
27. Liu, C. Q., Bakeri, H., Li, T. S. & Swaroop, A. Regulation of retinal progenitor expansion by Frizzled receptors: implications for microphthalmia and retinal coloboma. *Hum. Mol. Genet.* **21**, 1848–1860 (2012).

Acknowledgements

We thank A. Velasco and D. Waghray for assistance. GM/CA@APS has been funded in whole or in part with Federal funds from the National Cancer Institute (ACB-12002) and the National Institute of General Medical Sciences (AGM-12006). This research used resources of the Advanced Photon Source, a US Department of Energy (DOE) Office of Science User Facility operated for the DOE Office of Science by Argonne National Laboratory under contract no. DE-AC02-06CH11357. The Eiger 16 M detector was funded by an National Institutes of Health (NIH) Office of Research Infrastructure Programs, High-End Instrumentation Grant (1S10OD012289-01A1). The Berkeley Center for Structural Biology is supported in part by the Howard Hughes Medical Institute. The Advanced Light Source is a Department of Energy Office of Science User Facility under contract no. DE-AC02-05CH11231. Use of the SSRL, Stanford Linear Accelerator Center (SLAC) National Accelerator Laboratory, is supported by the US Department of Energy, Office of Science, Office of Basic Energy Sciences under contract no. DE-AC02-76SF00515. The SSRL Structural Molecular Biology Program is supported by the Department of Energy Office of Biological and Environmental Research, and by the NIH, National Institute of General Medical Sciences (including P41GM103393). The work here is supported by the Ludwig Foundation and Mathers Fund (K.C.G.), Howard Hughes Medical Institute (K.C.G. and D.B.) and NIH (grants U01DK085527, U19AI116484, R01NS100904, and U01CA217851 to C.J.K., and grant 1R01DK115728 to C.J.K. and K.C.G.).

Author contributions

L.T.D., Y.M., K.C.G., and D.B. conceived the project. L.T.D. computationally designed, optimized, and characterized DRPB_Fz8, and obtained site saturation mutagenesis data for specificity tuning. Y.M. constructed the Fz4/7 targeting library, performed yeast surface display selection, purified all proteins, determined complex structures, and performed cell line DRPB inhibition assays. A.H., K.Y., and N.H. performed duodenum organoid experiments and in vivo histology experiments. J.G.V. contributed to tissue collection and pathology assessment. M.V. and J.Y. packaged adenovirus. K.P. contributed to computational DRPB design. C.Y.J. generated the luciferase reporter cell line. K.M.J. contributed to crystallography data collection. K.M. contributed to yeast surface display selections. C.J.K. supervised the organoid experiments and in vivo experiments. K.C.G. and D.B. supervised the project and interpreted the data. L.T.D., Y.M., K.C.G., and D.B. wrote the manuscript with input from all authors.

Competing interests

K.C.G., D.B., Y.M., and L.T.D. are inventors on patent application 62/698576 submitted by Stanford University that covers the use of Frizzled-specific Wnt antagonists.

Additional information

Supplementary information is available for this paper at https://doi.org/10.1038/s41594-019-0224-z.

Reprints and permissions information is available at www.nature.com/reprints.

Correspondence and requests for materials should be addressed to K.C.G. or D.B.

Publisher's note: Springer Nature remains neutral with regard to jurisdictional claims in published maps and institutional affiliations.

Methods

Computational design and in vitro evolution by yeast surface display. Due to space considerations of the Methods section, the detailed protocol is included in the Supplementary Notes.

Biolayer interferometry. Data were collected with an Octet RED96 (FortéBio) instrument and analyzed with the ForteBio data analysis package. All experiments were performed at 20 °C in HBS-EP Buffer (GE Biosciences) with BSA blocking agent added (0.01 M HEPES, pH 7.4, 0.15 M NaCl, 3 mM EDTA, 0.005% v/v Surfactant P20, 1% BSA). Dip and Read Streptavidin Biosensors (FortéBio) were activated for 30 min in buffer prior to loading with biotinylated Fz5CRD (at 50 nM). After baseline reference collection, biosensors were dipped in analyte binder solutions to measure association and then returned to the empty buffer-containing baseline well to measure dissociation. Kinetic binding constants were determined after reference subtraction using a 1:1 binding model. Competition assays were carried out by loading the biosensors with biotinylated protein and then sequentially subjecting the biosensors to 250 nM (in HBS-EP Buffer) of protein A and then protein B (DRPB_Fz8, B12, Oncomed scFv or buffer)[14,20].

Circular dichroism. DRPB_Fz8 was dialyzed into PBS (20 mM $NaPO_4$, 150 mM NaCl) and analyzed at a final concentration of 12 mg ml^{-1}. Circular dichroism spectra were collected on an AVIV Model 420 CD spectrometer (AVIV Biomedical) using a 1 mm pathlength quartz cuvette. Scans were collected at 25 °C and were taken from 195 to 265 nm in 1 nm steps with 1 nm bandwidth at a scanning speed of 10 nm min^{-1}. Three independent scans were averaged and buffer subtracted against a cuvette holding PBS. Temperature melts were carried out with the same parameters from 25 °C to 95 °C in 1 °C steps, reading at 222 nm. During the melt, a full wavelength scan was taken at 25, 35, 45, 55, 65, 75, 85, and 95 °C using the parameters above.

Protein constructs, expression, and purification. All the DRPB protein sequences were cloned with a carboxy-terminal His-tag into pET28a vector. The vectors were transformed into BL21(DE3)pLysS cells (Life Technologies) and induced by 0.5 mM isopropyl-b-D-thiogalactoside (IPTG) at 16 °C for 16 h when the OD_{600} (optical density at 600 nm) reached 0.6. Cells were pelleted by centrifugation and lysed by sonication in lysis buffer (20 mM HEPES, pH 7.2, 300 mM NaCl). The proteins were purified by Ni^{2+}-nitrolotriacetic acid (NTA) affinity column chromatography followed by size exclusion chromatography via a Superdex S75 column (GE Healthcare) in HBS buffer (10 mM HEPES, pH 7.2, 150 mM NaCl). The MSA-DRPB proteins were expressed in High Five (*Trichoplusia ni*) cells (Invitrogen) using the baculovirus expression system. These proteins were purified similarly via a Superdex S200 column (GE Healthcare) in PBS buffer. Subsequently, endotoxin was removed following instructions for the Proteus NoEndoTM High Capacity Midi spin column kit (GEN-NoE12HC). Before administration, endotoxin levels were quantified using a Pierce LAL Chromogenic Endotoxin Quantitation Kit (catalog no. 88282). The proteins were also sterile filtered.

The CRDs of human Fz1 (residues 113–230), Fz4 (residues 42–161), Fz7 (residues 36–163) and Fz8 (residues 32–150 with N49Q mutation) used for crystallization containing a C-terminal 6× His-tag were expressed in High Five (*Trichoplusia ni*) cells (Invitrogen) using the baculovirus expression system. All proteins were secreted from High Five insect cells grown in Insect-Xpress medium (Lonza Pharma & Biotech), and purified using Ni^{2+}-NTA affinity column chromatography followed by size exclusion chromatography via a Superdex S75 column in HBS buffer. Similarly, The CRDs of these human Fzs were cloned with a C-terminal 3C protease cleavage site (LEVLFQ/GP), a biotin acceptor peptide (BAP)-tag (GLNDIFEAQKIEWHE) and a 6× His-tag and purified as described. These CRDs were site-specifically biotinylated using a BirA biotin-protein ligase standard reaction kit (Avidity, catalog no. BirA500). Successful biotinylation was confirmed by SDS-PAGE running Fz CRD side by side with Fz CRD mixed with SA.

Affinity measurements by surface plasmon resonance. Biotinylated Fz CRDs were coupled on a SA sensor chip (GE Healthcare) at low density with target RU increase of 120. An unrelated biotinylated protein was captured at equivalent coupling density to the control flow cells. Increasing concentrations of DRPB proteins were flown over the chip in HBS-P buffer (GE Healthcare) containing 10% glycerol and 0.05% BSA at 30 µl ml^{-1}. The chip surface was regenerated after each injection with 4 M $MgCl_2$. The measurements were conducted using a BIAcore T100 (GE Healthcare) and analyzed using the accompanying evaluation software.

Protein crystallization, data collection and structure determination and refinement. Individual DRPB-Fz CRD complexes were formed by mixing purified DRPB with Fz CRD at 1:1 molar ratio. The complex was further treated with 1:100 (w/w) carboxypeptidase A (Sigma C9286) and carboxypeptidase B (Sigma, C9584) overnight at 4 °C. The complex was further purified by size exclusion chromatography via a Superdex S75 column (GE Healthcare) in HBS buffer. The purified complex was concentrated using an Amicon Ultra concentrator (10 K MWCO, Millipore). Crystals were grown by sitting-drop vapor diffusion at 295 K.

The DRPB_Fz8–Fz8CRD complex protein was concentrated to 40 mg ml^{-1} in HBS buffer. Crystals showed up after one month in 0.2 M ammonium acetate, 0.1 M HEPES, pH 7.5, and 55% MPD. The DRPB_Fz4–Fz4CRD complex protein was concentrated to 40 mg ml^{-1} in HBS buffer. Crystals were present after 2 weeks in 0.2 M ammonium chloride, pH 6.3, and 20% PEG 3,350. The DRPB_Fz7/8–Fz7CRD complex protein was concentrated to 14 mg ml^{-1} in HBS buffer. Crystals showed up after 5 d in 0.1 M sodium acetate, pH 4.5, 2 M ammonium sulfate. The DRPB_Fz7–Fz7CRD complex protein was concentrated to 20 mg ml^{-1} in HBS buffer. Crystals showed up after 1 week in 0.2 M Na_2HPO_4: citric acid, pH 4.2, and 2 M ammonium sulfate.

X-ray intensity data sets were collected at the Advanced Light Source (ALS) 8.2.1 and 8.2.2 lines, Advanced Photon Source (APS) 23-ID-D line and Stanford Synchrotron Radiation Lightsource (SSRL) 12–2 line. Data were indexed and scaled using XDS[28] or HKL 2000 (ref. [29]). The DRPB_Fz8–Fz8CRD structure with was determined by molecular replacement using Phaser. The Rosetta-calculated DRPB_Fz8 structure and the Fz8CRD (PDB: 4F0A[15]) structure were used as the search models. Similarly, the other structures were determined using their respective Fz CRD model (PDB: 5BPB and 5T44). All structures were manually built in Coot[30] and improved by multiple rounds of refinement in Phenix[31] and manual rebuilding. Detailed statistics for data collection and refinement are reported in Table 1. These structures are deposited at the PDB under accession codes: 6NDZ, 6NE1, 6NE2, and 6NE4, with 97.3%, 95.6%, 98.4%, and 98.1% Ramachandran favored residues and no Ramachandran outliers, respectively.

Fz-specific inhibition using luciferase assay. HEK293T and A375 cells were stably transfected with the luciferase reporter and a constitutively expressed *Renilla* luciferase as reported previously[20], denoted as HEK293STF and A375BAR. BeWo cells were stably transfected with lentiviral transfection expressing firefly luciferase reporter as described previously[20]. The assay measurements were performed using the Dual Luciferase Assay kit (Promega, E1960) as instructed. The A375BAR cell line was used as the Fz2 predominant cell line and the BeWo (ATCC) cell line was used as the Fz5 predominant cell line. In brief, 10,000 to 20,000 cells were plated to each well in a 96-well sterile cell culture plate the first day. The next day, cells were pre-incubated with different concentrations of DRPBs for 1 h. The cells were subsequently stimulated with 20% Wnt3a conditioned media (ATCC) with 25 nM R-spondin protein for another 20 h. In Fz4 inhibition assays, a Fz4 predominant cell line was difficult to isolate. Therefore, HEK293STF cells were plated at a density of 15,000 cells per well on the first day. On the second day, the cells were transfected with human Fz4 receptor using Fugene HD (Promega) following the manufacturer's protocol. On the third day, the cells were pre-incubated with 20 nM DRPB_Fz7/8 (previously shown to fully inhibit Fz7 subtype and Fz8 subtype mediated Wnt signaling) and different concentrations of DRPB_Fz4 for 1 h. Therefore, the luciferase signaling output in these cells was only mediated by Fz4 receptors. The cells were subsequently stimulated with 20% Wnt3a conditioned media and 25 nM R-spondin for another 20 h before analysis. These cells were washed with PBS buffer (Thermo Fisher, 10010023) and lysed as instructed in the Dual Luciferase Assay kit (Promega) user manual. Luminance signals were recorded using the SpectraMax Paradigm (Molecular Dimensions). The data were analyzed by GraphPad Prism 7.

Organoid culture assay. Mouse duodenal organoids were derived from adult C57BL/6 J mice (Jackson Laboratory, ME, USA) using the method described before[32]. Human duodenal organoids were established from de-identified surgical discards. Primary tissues were obtained through the Stanford Tissue Bank from patients undergoing surgical resection at Stanford University Medical Center (SUMC). All experiments utilizing human material were approved by the SUMC Institutional Review Board. Written informed consent for research was obtained from donors prior to tissue acquisition. For the 3D cultures, Matrigel (BD Biosciences) was used and overlaid with a liquid medium consisting of DMEM/F12 advanced medium (Invitrogen), supplemented with additional factors including EGF (50 ng/ml), Noggin (100 ng/ml), and RSPO (500 ng/ml). Medium was replenished every 3 d.

In vivo experiments. Adult C57BL/6J mice (Jackson Laboratory) between 9 and 10 weeks old were injected intravenously with recombinant proteins (15 mg kg^{-1} daily) or adenoviruses (single dose of 1×10^9 plaque-forming units (pfu) per mouse). Intestinal tissues were collected and fixed in 4% paraformaldehyde (Fig. 4b) or 10% formalin (Fig. 4c–g). For H&E staining of jejunum cross-sections (Fig. 4b,c) and immunofluorescence staining of livers (Fig. 4d), we used mice that received adenoviruses expressing mouse IgG Fc (Fc) or different Fz subtype-specific DRPB antagonist, 7 d post adenovirus injection ($n = 6$ to $n = 9$ mice per group). Paraffin-embedded sections were stained with mouse anti-glutamine synthetase (GS) antibody (Millipore, MAB302, 1:50) following citrate antigen retrieval and blocking with 5% normal goat serum. The immunostained tissue sections were analyzed and images were captured on a fluorescence microscope (KEYENCE, BZ-X710). For GS quantification, 3 pictures at ×10 magnification from each section were analyzed using ImageJ, quantifying the integrated density of the area (100 µm × 100 µm) around the central vein. Four areas were measured in each picture. The average of the integrated density was normalized by Ad-Fc control. Serum expression of Ad-Fz subtype-specific DRPB antagonists (DRPB_Fz4,

DRPB_Fz7, DRPB_Fz8 and DRPB_Fz7/8) were confirmed by immunoblotting using mouse anti-6×His (Abcam, ab18184). All experiments used $n=6$ to $n=9$ mice per group and were repeated twice. All animal experiments were conducted in accordance with procedures approved by the IACUC at Stanford University.

Mouse liver RNA isolation, cDNA synthesis, and qPCR. A small portion of liver from each mouse was cut and placed in RNAlater stabilization solution (Invitrogen). Total RNA was isolated using TRIzol Reagent (Life Technologies) and a Direct-Zol MiniPrep Kit (Zymo). Complemetnary DNA was generated from 500 ng of RNA using iScript Reverse Transcription Supermix for qRT-qPCR) (Bio-Rad). Quantitative PCR (qPCR) was performed on a total of 5.6 ng of cDNA per sample using Power SYBR Green PCR Master Mix (Applied Biosystems) on the CFX384 Real-Time System (Bio-Rad). Fold changes in gene expression were calculated using the Ct method from Ct values normalized to Gapdh on Microsoft Excel and Prism. Primer sequences for each gene were published as follows:

Mouse GS F: 5′-ATGCAGATAGGGTGACCACT-3′
Mouse GS R: 5′-GTCCATTTGCAGGAAATGGC-3′
Mouse Axin2 F: 5′-GCAGGAGCCTCACCCTTC-3′
Mouse Axin2 R: 5′-TGCCAGTTTCTTTGGCTCTT-3′
Mouse Gapdh F: 5′-CCCCAATGTGTCCGTCGTG-3′
Mouse Gapdh R: 5′-GCCTGCTTCACCACCTTCT-3′

Statistical analysis. Statistical analysis was performed using the GraphPad Prism software. All statistical tests use biological replicates and are indicated by group size (n) in the figure legend. Results are expressed as mean + s.e.m. Two-sided P values were calculated by Dunn's test of multiple comparisons following the Kruskal-Wallis test. *$P<0.05$, ** $P<0.01$, ****$P<0.0001$.

Reporting Summary. Further information on research design is available in the Nature Research Reporting Summary linked to this article.

Data availability

The structures are deposited in the Protein Data Bank under accession codes 6NDZ, 6NE1, 6NE2, and 6NE4. Other data are available from corresponding authors upon reasonable request.

References

28. Kabsch, W. Integration, scaling, space-group assignment and post-refinement. *Acta Crystallogr. D* **66**, 133–144 (2010).
29. Otwinowski, Z. & Minor, W. in *Methods in Enzymology* Vol. 276 (New York: Academic Press, 1997).
30. Emsley, P., Lohkamp, B., Scott, W. G. & Cowtan, K. Features and development of Coot. *Acta Crystallogr. D* **66**, 486–501 (2010).
31. Afonine, P. V. et al. Towards automated crystallographic structure refinement with phenix. refine. *Acta Crystallogr. D* **68**, 352–367 (2012).
32. Sato, T. et al. Single Lgr5 stem cells build crypt-villus structures in vitro without a mesenchymal niche. *Nature* **459**, 262–265 (2009).

nature research

Corresponding author(s): David Baker and K. Christopher Garcia

Last updated by author(s): Mar 19, 2019

Reporting Summary

Nature Research wishes to improve the reproducibility of the work that we publish. This form provides structure for consistency and transparency in reporting. For further information on Nature Research policies, see Authors & Referees and the Editorial Policy Checklist.

Statistics

For all statistical analyses, confirm that the following items are present in the figure legend, table legend, main text, or Methods section.

n/a	Confirmed	
☐	☒	The exact sample size (*n*) for each experimental group/condition, given as a discrete number and unit of measurement
☐	☒	A statement on whether measurements were taken from distinct samples or whether the same sample was measured repeatedly
☐	☒	The statistical test(s) used AND whether they are one- or two-sided *Only common tests should be described solely by name; describe more complex techniques in the Methods section.*
☐	☒	A description of all covariates tested
☒	☐	A description of any assumptions or corrections, such as tests of normality and adjustment for multiple comparisons
☐	☒	A full description of the statistical parameters including central tendency (e.g. means) or other basic estimates (e.g. regression coefficient) AND variation (e.g. standard deviation) or associated estimates of uncertainty (e.g. confidence intervals)
☒	☐	For null hypothesis testing, the test statistic (e.g. *F*, *t*, *r*) with confidence intervals, effect sizes, degrees of freedom and *P* value noted *Give P values as exact values whenever suitable.*
☒	☐	For Bayesian analysis, information on the choice of priors and Markov chain Monte Carlo settings
☒	☐	For hierarchical and complex designs, identification of the appropriate level for tests and full reporting of outcomes
☒	☐	Estimates of effect sizes (e.g. Cohen's *d*, Pearson's *r*), indicating how they were calculated

Our web collection on statistics for biologists contains articles on many of the points above.

Software and code

Policy information about availability of computer code

Data collection	Design structures were generated and collected using the Rosetta macromolecular modeling suite and the Patchdock protein-protein docking software. The flow cytometry data was collected using BD Accuri C6 with Sampler using accompanying software. Yeast FACS sorting was performed using SONY Cell Sorter SH800S using SONY accompanying software. The macromolecular crystallography data was collected at synchrotron using provided software. The Luciferase signaling data was collected with Molecular Devices SpectraMax Paradigm using accompanying Soft MaxPro 6.2.1. software. The surface plasmon resonance data was collected on Biacore T100 using accompanying control software. The biolayer inferometry data was collected with the Octet RED96 (ForteBio) instrument utilizing the accompanying software. The Organoid assay and H&E stained tissue sections were imaged using the microscope (KEYENCE BZ-X710). The immunostained tissue sections were captured using KEYENCE BZ-X710.
Data analysis	Statistical analysis was performed using Microsoft Excel, GraphPad Prism 6 or GraphPad Prism 7. Protein design and structural analysis was performed utilizing the Rosetta macromolecular modeling suite. Protein visualization and structure image processing were performed using PyMol and Foldit. Flow cytometry data was analyzed by the accompanying BD Accuri C6 software. The macromolecular crystallography data was analyzed and processed using softwares including HKL2000, XDS, PHENIX and Coot as detailed in the Method sections. The surface plasmon resonance data was analyzed using Biacore T100 accompanying evaluation software. The biolayer inferometry data was analyzed utilizing accompanying ForteBio data analysis software. Immunofluorescence images were quantified by Image J.

For manuscripts utilizing custom algorithms or software that are central to the research but not yet described in published literature, software must be made available to editors/reviewers. We strongly encourage code deposition in a community repository (e.g. GitHub). See the Nature Research guidelines for submitting code & software for further information.

Data

Policy information about availability of data

All manuscripts must include a data availability statement. This statement should provide the following information, where applicable:

- Accession codes, unique identifiers, or web links for publicly available datasets
- A list of figures that have associated raw data
- A description of any restrictions on data availability

The crystal structures are deposited in Protein Data Bank under the accession codes 6NDZ, 6NE1, 6NE2 and 6NE4.

Field-specific reporting

Please select the one below that is the best fit for your research. If you are not sure, read the appropriate sections before making your selection.

☒ Life sciences ☐ Behavioural & social sciences ☐ Ecological, evolutionary & environmental sciences

For a reference copy of the document with all sections, see nature.com/documents/nr-reporting-summary-flat.pdf

Life sciences study design

All studies must disclose on these points even when the disclosure is negative.

Sample size	Group sample sizes were chosen based on previous experiments and in order to perform statistics analysis.
Data exclusions	No Data were excluded from the analyses.
Replication	All experiments, unless otherwise stated, have been replicated with similar results, the details can be found in the manuscript.
Randomization	Mice were randomly allocated into experimental groups.
Blinding	There was no blinding in the experiments. Each experiment was performed by a single experimentalist. Given proper sample handling and data analysis by computer-based methods, blinding would not have effects on experiments, e.g. protein structure determination and flow cytometry.

Reporting for specific materials, systems and methods

We require information from authors about some types of materials, experimental systems and methods used in many studies. Here, indicate whether each material, system or method listed is relevant to your study. If you are not sure if a list item applies to your research, read the appropriate section before selecting a response.

Materials & experimental systems

n/a	Involved in the study
☐	☒ Antibodies
☐	☒ Eukaryotic cell lines
☒	☐ Palaeontology
☐	☒ Animals and other organisms
☒	☐ Human research participants
☒	☐ Clinical data

Methods

n/a	Involved in the study
☒	☐ ChIP-seq
☐	☒ Flow cytometry
☒	☐ MRI-based neuroimaging

Antibodies

Antibodies used	Myc-Tag (9B11) Mouse mAb (Alexa Fluor® 488 Conjugate) Cell signaling #2279, Lot#18, 1:100 dilution; Myc-Tag (9B11) Mouse mAb (Alexa Fluor® 647 Conjugate) Cell signaling #2233, Lot#19, 1:100 dilution; Mouse anti-glutamine synthetase (GS) antibody (Millipore #MAB302),Lot#2795087, 1:50 dilution
Validation	All antibodies used in this study are commercially available and validated by the manufacturer. The detailed information can be found on respective website. Listed below is representative publication provided by the manufacturer. Myc-Tag (9B11) Mouse mAb (Alexa Fluor® 488 Conjugate) previous citation: Yan, Kelley S., et al. "Non-equivalence of Wnt and R-spondin ligands during Lgr5+ intestinal stem-cell self-renewal." Nature 545.7653 (2017): 238. Mouse anti-glutamine synthetase (GS) antibody previous publication: Niu, Wenze, et al. "SOX2 reprograms resident astrocytes into neural progenitors in the adult brain." Stem cell reports 4.5 (2015): 780-794. Myc-Tag (9B11) Mouse mAb (Alexa Fluor® 647 Conjugate) previous citation: Hill, Zachary B., et al. "Human antibody-based

chemically induced dimerizers for cell therapeutic applications." Nature chemical biology 14.2 (2018): 112.

Eukaryotic cell lines

Policy information about cell lines

Cell line source(s)	HEK293STF and A375BAR in this manuscript were previously reported and used by the Garcia lab: Janda, Claudia Y., et al. "Surrogate Wnt agonists that phenocopy canonical Wnt and β-catenin signalling." Nature 545.7653 (2017): 234. BeWo cells were purchased from ATCC.
Authentication	The Frizzled expression profile was reported in (Janda, Claudia Y., et al. "Surrogate Wnt agonists that phenocopy canonical Wnt and β-catenin signalling." Nature 545.7653 (2017): 234.). No further authentication was performed by the authors.
Mycoplasma contamination	Cell lines were not tested for mycoplasma contamination by authors.
Commonly misidentified lines (See ICLAC register)	None

Animals and other organisms

Policy information about studies involving animals; ARRIVE guidelines recommended for reporting animal research

Laboratory animals	Adult C57Bl/6J male mice between 9-10 weeks
Wild animals	The study did not involve wild animals.
Field-collected samples	The study did not involve samples collected from the filed.
Ethics oversight	All animal experiments were conducted in accordance with procedures approved by the IACUC at Stanford University.

Note that full information on the approval of the study protocol must also be provided in the manuscript.

Flow Cytometry

Plots

Confirm that:

☒ The axis labels state the marker and fluorochrome used (e.g. CD4-FITC).

☒ The axis scales are clearly visible. Include numbers along axes only for bottom left plot of group (a 'group' is an analysis of identical markers).

☐ All plots are contour plots with outliers or pseudocolor plots.

☒ A numerical value for number of cells or percentage (with statistics) is provided.

Methodology

Sample preparation	Please refer to Methods
Instrument	Yeast surface display: BD Accuri C Sampler
Software	Yeast surface display: BD Accuri C Sampler accompanying software
Cell population abundance	There is only a single population of EBY100 yeast.
Gating strategy	The yeast cell gating was first based on forward/side scattering. The singlets were further gated using forward scattering area versus height.

☐ Tick this box to confirm that a figure exemplifying the gating strategy is provided in the Supplementary Information.